

## ARTICLE OPEN

Electronic structure and exciton shifts in Sb-doped MoS<sub>2</sub> monolayerMianzeng Zhong<sup>1,2</sup>, Chao Shen<sup>1</sup>, Le Huang<sup>3</sup>, Hui-Xiong Deng<sup>1</sup>, Guozhen Shen<sup>1</sup>, Houzhi Zheng<sup>1</sup>, Zhongming Wei<sup>1</sup> and Jingbo Li<sup>1</sup>

The effective manipulation of excitons is important for the realization of exciton-based devices and circuits, and doping is considered a good strategy to achieve this. While studies have shown that 2D semiconductors are ideal for excitonic devices, preparation of homogenous substitutional foreign-atom-doped 2D crystals is still difficult. Here we report the preparation of homogenous monolayer Sb-doped MoS<sub>2</sub> single crystals via a facile chemical vapor deposition method. A and B excitons are observed in the Sb-doped MoS<sub>2</sub> monolayer by reflection magnetic circular dichroism spectrum measurements. More important, compared with monolayer MoS<sub>2</sub>, the peak positions of two excitons show obvious shifts. Meanwhile, the degeneration of A exciton is also observed in the monolayer Sb-doped MoS<sub>2</sub> crystal using photoluminescence spectroscopy, which is ascribed to the impurity energy levels within the band-gap, confirmed by density function theory. Our study opens a door to developing the doping of 2D layered transition metal dichalcogenides with group-V dopants, which is helpful for the fundamental study of the physical and chemical properties of transition metal dichalcogenides.

npj 2D Materials and Applications (2019)3:1 ; <https://doi.org/10.1038/s41699-018-0083-1>

## INTRODUCTION

The large exciton binding energy and long exciton diffusion length make the two-dimensional (2D) semiconductors become an ideal system for realizing the practical exciton-based devices operating at room-temperature.<sup>1,2</sup> Among them, 2D MoS<sub>2</sub> as a typically layered transition metal dichalcogenides (TMDCs) has received increasing attention due to its unique physical and chemical properties, and potential applications in electronic and optical fields.<sup>3–5</sup> Especially, the theories and experiments have shown that monolayer MoS<sub>2</sub> has more attractive properties than its bulk form.<sup>6–11</sup> For example, a direct band gap,<sup>6,8</sup> valley Hall effect,<sup>7,9</sup> and the inversion symmetry breaking have been observed in monolayer MoS<sub>2</sub>.<sup>10,11</sup> Many methods have developed to synthesize monolayer MoS<sub>2</sub>, among them the most efficient methods are liquid phase exfoliation, mechanical exfoliation, and chemical vapor deposition.<sup>12–14</sup> Very recently, the monolayer MoS<sub>2</sub>, which synthesized by the mechanical exfoliated method, based field effect transistors show a high electronic mobility up to 200 cm<sup>2</sup>/V·s at room temperature, a large on/off current ratio of about 10<sup>8</sup>, and low standby power dissipation.<sup>13</sup> But, it is hardly applicable to the large-scale practical devices, due to the low-yield and poor controllability of the mechanical exfoliation technology.<sup>3</sup> To this end, how to grow the large-scale monolayer MoS<sub>2</sub> crystals with high electronic mobility is an important research topic in recent years. Several groups have succeeded in the preparation of monolayer MoS<sub>2</sub> crystals by the CVD method. As reported, the growth precursors and recipes have a direct influence on the electronic properties of the prepared samples. The obtained electronic mobility ranges from less than 1 to about 90 cm<sup>2</sup>/V·s at room temperature, which are directly related to the density of

defects in samples.<sup>14–18</sup> Meanwhile, elements doping is considered as a good way to regulate the physical properties of MoS<sub>2</sub>; it can change the electronic band structure of the pristine materials, as a result, it affects the transport of electrons.

For semiconducting materials, it is a good strategy to control their basic physical properties, such as the conduction type, carrier concentration, electrical conductivity, band gap, and photoluminescence, by impurity doping. Several groups have studied the possibility of other species doping of monolayer MoS<sub>2</sub> by first-principles calculation method. The results show that the MoS<sub>2</sub> system is stable for the implant of group-VB (V, Nb), group-VIB (W, Cr), group-VIIB (Mn, Re), group-VIII (Fe, Co, Pd), group-IB (Au), group-IIIB (Zn, Cd, Hg), and group-VIA (Se) atoms;<sup>19–24</sup> meanwhile, monolayer MoS<sub>2</sub> doped by V, Cr, Mn, Fe, Co, Zn, Cd and Hg atoms exhibit magnetic states.<sup>20,23,24</sup> Following the theoretical prediction that monolayer MoS<sub>2</sub> would have more interesting physical properties by impurity doping, intensive experimental works have been done on doped monolayer MoS<sub>2</sub>. For example, Zn and Nb-doped MoS<sub>2</sub> crystals exhibit p-type transport properties;<sup>25,26</sup> the optical energy gap of MoS<sub>2</sub> can be controllably modulated by the implant of W and Se atoms;<sup>27–30</sup> rare-earth Er-doped MoS<sub>2</sub> thin films show up-conversion and down-conversion PL emissions located in near infrared reflection spectral region;<sup>31</sup> additionally, other elements doping of MoS<sub>2</sub> have been also experimentally achieved, such as Co, Re, Cr, V, and Mn.<sup>32–35</sup> The inhomogenous doping of crystals and the enhanced impurity scattering to electrons hinder the development of elements doping of MoS<sub>2</sub>. The suitable dopants and growth recipes are essential for the improvement of the intrinsic properties of MoS<sub>2</sub> crystals. Group-VA based compound semiconductors, which exhibit excellent

<sup>1</sup>State Key Laboratory of Superlattices and Microstructures, Institute of Semiconductors, Chinese Academy of Sciences & Center of Materials Science and Optoelectronics Engineering, University of Chinese Academy of Sciences, Beijing 100083, China; <sup>2</sup>Hunan Key Laboratory of Super-microstructure and Ultrafast Process, School of Physics and Electronics, Central South University, Changsha 410083, China and <sup>3</sup>School of Materials and Energy, Guangdong University of Technology, Guangzhou, Guangdong 510006, China

Correspondence: Zhongming Wei (zmwei@semi.ac.cn)

Received: 23 August 2018 Accepted: 8 November 2018

Published online: 04 January 2019

carrier transport properties, are the important materials for the applications in microelectronics.<sup>36,37</sup> Meanwhile, a recent theory research shows that the surface S atoms substitute by the group-VA elements (N and P) may result in MoS<sub>2</sub> become a p-type semiconductor with magnetic.<sup>21</sup> More important, there is no report about the successful preparation of the homogenous group-VA elements doped MoS<sub>2</sub> single crystals.

Here, we prepared the monolayer Sb-doped MoS<sub>2</sub> single crystals by a facile chemical vapour deposition (CVD) method. The growth time and the carrier gas flow rate affect the final morphology of crystals. The synthesized crystals exhibit high-quality, single crystalline, and homogenous composition which are confirmed by aberration-corrected scanning transmission electron microscopy (AC-STEM), energy dispersive X-ray spectroscopy (EDS), and Raman mappings. The quantitative analysis of the EDS spectrum further confirmed the crystals are monolayer Mo<sub>0.91</sub>Sb<sub>0.09</sub>S<sub>2</sub> nanosheet. The shifts of A and B excitons are also observed in the monolayer Sb-doped MoS<sub>2</sub> nanosheets which measured by RMCD.

## RESULTS

### Growth and characterization of monolayer Sb-doped MoS<sub>2</sub> nanosheets

For the growth of MoS<sub>2</sub> and Sb-doped MoS<sub>2</sub> nanosheets, a facile CVD process was used. As illustrated in Supplementary Figure S1a, two ceramic boats loaded with molybdenum trioxide powder and antimony powder were placed at the high-temperature zone of the furnace, respectively; and another boat loaded with sulfur was placed at the inlet of the tube. The SiO<sub>2</sub>/Si (the thickness of SiO<sub>2</sub> is 300 nm) wafer was selected as the substrate, which was placed on the top of the ceramic boat loaded with MoO<sub>3</sub> powder. Before heating, high-purity Ar carrier gas was first introduced into the tube flow at 150 sccm for 30 min to eliminate air in growth system, then the flow of Ar gas decrease to 5 sccm. The furnace was then heated from room temperature to 955 K at a rate of 36 K/min, and the temperature was kept at 955 K for 1 min. After 1 min of growth at 955 K, open the upper cover of the furnace to let it naturally cooled to room temperature. The detailed changes of temperature at different stages for growth process were summarized in Supplementary Figure S1b. The optical micrograph (OM) and atomic force microscopy (AFM) images of an as-synthesized representative MoS<sub>2</sub> sample fabricated with a growth time of 1 min show in Supplementary Figure S2.

Figure 1a is an OM of an as-synthesized representative Sb-doped MoS<sub>2</sub> sample fabricated with a growth time of 1 min, which shows that the crystals are triangle-shaped nanosheets with the edge lengths of 30–60 μm. The achieved triangle-shaped nanosheets have a smooth surface, regular structure, and homogeneous contrast, as shown in Fig. 1b (a magnified OM of a typical Sb-doped MoS<sub>2</sub> nanosheet). Meanwhile, a typical AFM image also exhibits homogeneous contrast, indicating Sb-doped MoS<sub>2</sub> nanosheet has a highly smooth surface. The height profile (Fig. 1c) shows the thickness of the typical nanosheet is about 0.79 nm, which corresponds to monolayer MoS<sub>2</sub>. In the growth process, we found that the growth time directly affected the thickness and size of the final achieved crystals. Supplementary Figure S3a–c show typical OM of three typical samples after growing 30 s, 2 min, and 5 min, respectively. It is noting that their lateral size increases with growth time. After growth 5 min, the proportion of multilayer crystals increased significantly. The increase of the lateral size of crystals is mainly due to the dangling bonds exist on the edge of the crystals. The increase of the thickness of the as-prepared crystals with prolonging the growth time is due to the nuclei easier formed on the surface of crystals. Then the nuclei grow up to form new crystals, resulting in the forming of multilayer-structured crystals. In addition, we found

the carrier gas flow is also an important parameter in controlling the morphology of the final crystals. Under the small carrier gas flow (<5 sccm), the vapor pressure of sulfur can't be effectively formed in the substrate area. That is to say, there is not enough sulfur vapor to move to the substrate area in 1 min under a small carrier gas flow. It results in the formation of rhombic MoOS crystals (see Supplementary Figure S4a). However, when the flow carrier gas is larger than 40 sccm, some irregular crystals formed on the substrate (see Supplementary Figure S4b). This is mainly due to the sulfur molecules have a large movement rate and no effective residence time on the substrate zone.

The crystal structure, crystal quality, and chemical composition of the prepared Sb-doped MoS<sub>2</sub> crystals were investigated by AC-STEM, transmission electron microscopy (TEM), high-resolution TEM (HRTEM), selected-area electron diffraction (SAED) and energy dispersive X-ray spectroscopy (EDS). Supplementary Figure S5a shows the morphology of a typical triangle Sb-doped MoS<sub>2</sub> crystal, and all corresponding studies in this section based on this crystal. Atomic-resolution Z-contrast imaging was carried out to clarify the arrangement of the doped Sb in the MoS<sub>2</sub> crystal. An as-recorded scanning transmission electron microscope annular dark field (STEM-ADF) image is shown in Fig. 1d. The corresponding atomic model is shown in Fig. 1g. Due to the difference of atomic number in Mo, Sb, and S, the atoms show the different Z-contrast in STEM-ADF image. From STEM-ADF image, some different brightness spots (which depends on the Z-contrast, the brighter spot represents the atom has a larger number) can be clearly distinguished. These all spots with different intensities correspond to Sb, Mo, and S atoms, respectively, which can be further confirmed by the experimental intensity profile (Fig. 1e). All atoms are marked in Fig. 1d. The HRTEM of this nanosheet is shown in Supplementary Figure S6. The lattice spacing along different directions are 2.82 and 1.61 Å, which are corresponding to the {100} and {110} planes of 2H-MoS<sub>2</sub>, respectively. The crystallinity and crystallographic orientation of Sb-doped MoS<sub>2</sub> crystal are further confirmed by the SAED patterns. As shown in Fig. 1h, the SAED pattern taken from [001] zone axis shows a single set of diffraction spots with six-fold symmetry, which confirm a high quality and hexagonal structured single crystal. Meanwhile, the STEM-ADF image (Fig. 1i) of purity monolayer MoS<sub>2</sub> which synthesized under the same conditions with the Sb doped MoS<sub>2</sub>, show that the MoS<sub>2</sub> has good crystal quality. Furthermore, according to Figs. 1d, i, the doping of Sb atoms in MoS<sub>2</sub> does not make significant changes in lattice spacing of STEM-ADF patterns. The raw EDS spectrum collected from the nanosheet marked a white rectangle in Supplementary Figure S5a is shown in Supplementary Figure S7. It can be seen that the crystal is composed of Mo, Sb, and S (the detected C and Cu elements originate from the copper grid), and the stoichiometric ratio of Mo, Sb and S is about 0.91:0.09:2, indicating the composition of the nanosheet crystal as Mo<sub>0.91</sub>Sb<sub>0.09</sub>S<sub>2</sub>. The EDS mapping was performed to characterize the distribution of Mo, Sb, and S in nanosheet. Supplementary Figure S5b–d shows the corresponding elemental mapping for S, Sb, and Mo in a selected region of a typical crystal which marked with a white rectangle in Supplementary Figure S5a. It is shown that the S, Sb, and Mo elements are homogeneously distributed across the whole collected region; indicating that the Sb atom can be uniformly doped into the crystal. Supplementary Figure S8 is the X-ray photoelectron spectroscopy (XPS) result of the as-prepared sample. It can be seen that the Sb 3d core-level binding energy peaks occur in the prepared sample. The Sb 3d<sub>5/2</sub> and Sb 3d<sub>3/2</sub> signatures are located at 530.5 and 539.8 eV, which are similar to the energy peaks of Sb<sup>3+</sup>.<sup>38</sup> The TEM and XPS results provide clear evidences that Sb atoms are doped into MoS<sub>2</sub> lattice.

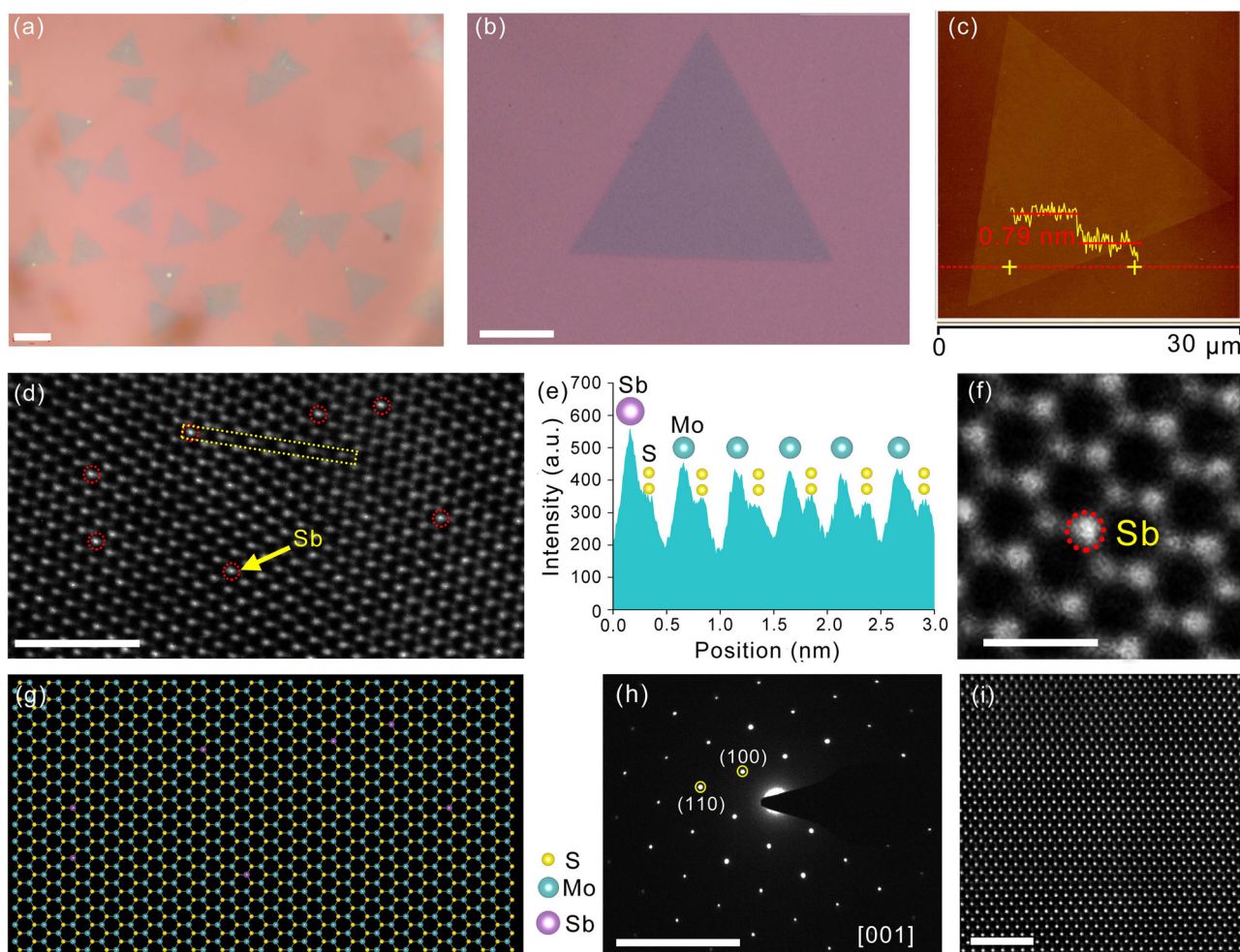


**Fig. 1** Growth and characterization of prepared crystals. **a** Optical image of monolayer Sb-doped MoS<sub>2</sub> crystals at low magnification. Scale bar = 40 μm. **b** Magnified optical image of a Sb-doped MoS<sub>2</sub> crystal. Scale bar = 20 μm. **c** A typical AFM image of a Sb-doped MoS<sub>2</sub> crystal, the thickness is 0.79 nm. **d** STEM-ADF image of a typical monolayer Sb-doped MoS<sub>2</sub> nanosheet, the Sb atoms have been marked. Scale bar = 2 nm. **e** Intensity profile of the selected line (bright yellow) in **d**. **f** Magnified image of the small area in **d**. Scale bar = 0.5 nm. **g** The corresponding atomic model of **d**. **h** The SAED pattern of this typical monolayer Sb-doped MoS<sub>2</sub> nanosheet. Scale bar = 10 1/nm. **i** STEM-ADF image of a typical monolayer MoS<sub>2</sub>. Scale bar = 2 nm.

#### Optical properties of monolayer Sb-doped MoS<sub>2</sub> nanosheets

The successful doping of Sb atom into the MoS<sub>2</sub> system was further confirmed by Raman spectroscopy and photoluminescence (PL) technology. Previous studies have proved that Raman spectroscopy technology is a powerful tool in determining the doping of TMDCs.<sup>25–28,30–32,35</sup> Fig. 2a is the optical image of as-prepared monolayer Sb-doped MoS<sub>2</sub> nanosheet on the SiO<sub>2</sub>/Si substrate. Figure 2b shows the corresponding Raman spectrum. Three Raman peaks located at 148, 383, and 401.7 cm<sup>-1</sup> are detected. Among them, 383 and 401.7 cm<sup>-1</sup> are assigned to in-plane E<sub>2g</sub> mode and out-of-plane A<sub>1g</sub> mode of MoS<sub>2</sub>. However, these two vibration modes show slightly shifts when compared with the purity monolayer MoS<sub>2</sub> nanosheet.<sup>3</sup> The Raman spectroscopy of purity monolayer MoS<sub>2</sub> nanosheet is also given in Fig. 2b, two typical vibration modes located at 383.6 and 401 cm<sup>-1</sup>, respectively. The shift of these two Raman peaks is mainly due to the doping of Sb atoms affect the original lattice vibration states. In addition, the peak located at 148 cm<sup>-1</sup> may be related to Sb<sub>x</sub>S<sub>y</sub>.<sup>39</sup>

Figures 2d–f show the Raman peak intensity mapping images of the peak centered at 148 cm<sup>-1</sup> (the mode related to Sb<sub>x</sub>S<sub>y</sub>),

383 cm<sup>-1</sup> (E<sub>2g</sub> mode of MoS<sub>2</sub>), and 401.7 cm<sup>-1</sup> (A<sub>1g</sub> mode of MoS<sub>2</sub>), respectively. It can be seen that three modes have the strong intensity and uniform color contrast. Therefore, the prepared nanosheet is a uniform Sb-doped MoS<sub>2</sub> crystal. Figure 2c is the PL results of monolayer Sb-doped MoS<sub>2</sub> nanosheet and purity monolayer MoS<sub>2</sub> nanosheet. Only A exciton is observed in PL results. The typical PL emission of MoS<sub>2</sub> located at 666 nm, which corresponding to the A exciton. When Sb atoms doped into MoS<sub>2</sub> to form Mo<sub>0.91</sub>Sb<sub>0.09</sub>S<sub>2</sub> crystals, the A exciton peak is red-shift from 666 to 687 nm. Meanwhile, the A exciton intensity becomes weaker and full width at half maximum becomes larger, respectively. The changes of A exciton are mainly due to the effect of Sb atoms to electronic band structure. The observed red-shift in A exciton for the Sb-doped MoS<sub>2</sub> samples mainly originates from the decrease of electronic bandgap. When the foreign Sb doped in the MoS<sub>2</sub>, the impurity energy levels will form in the electronic band. As a result, it decreases the electronic bandgap of MoS<sub>2</sub>. So, the combination of excited electron-hole pairs will produce photons with smaller energy. More detailed discussion has been given in the theory section.

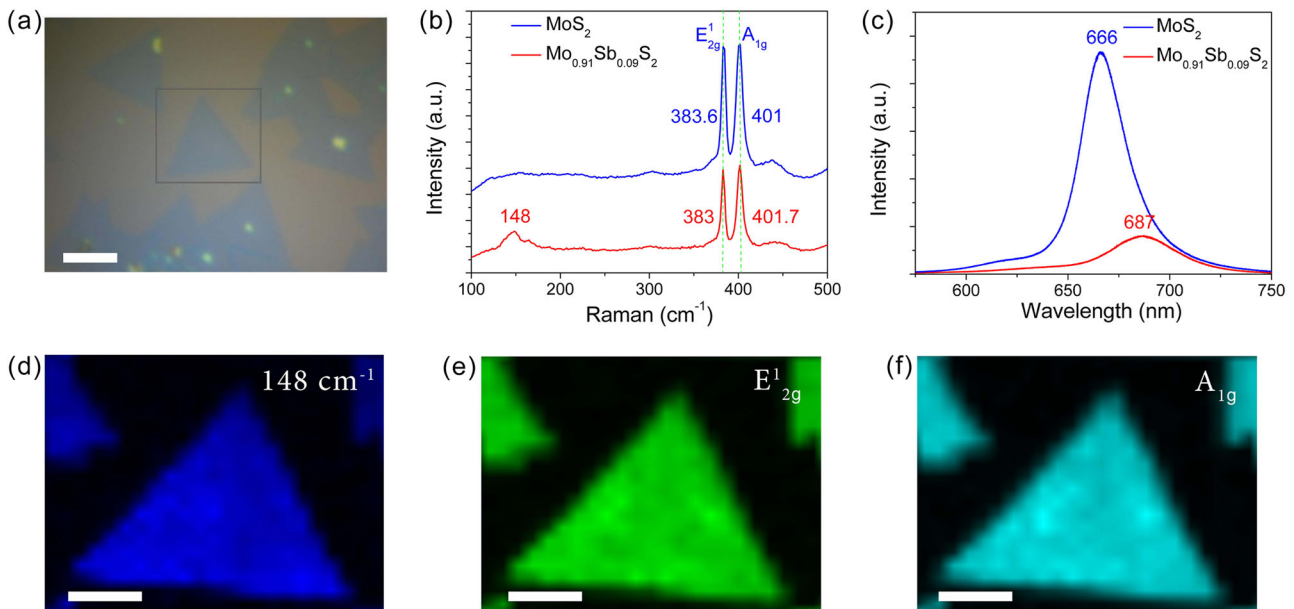


**Fig. 2** Raman and photoluminescence properties. **a** Optical image of the typical Sb-doped MoS<sub>2</sub> nanosheets collected from Raman spectra equipment CCD detector. Scale bar = 20  $\mu\text{m}$ . **b**, and **c** Raman, and photoluminescence spectra of monolayer Sb-doped MoS<sub>2</sub> and MoS<sub>2</sub> crystals. **d-f** Raman peak intensity mappings at 148, 383, and 401.7  $\text{cm}^{-1}$ , which collected from the marked square area in **a**. Scale bars = 10  $\mu\text{m}$

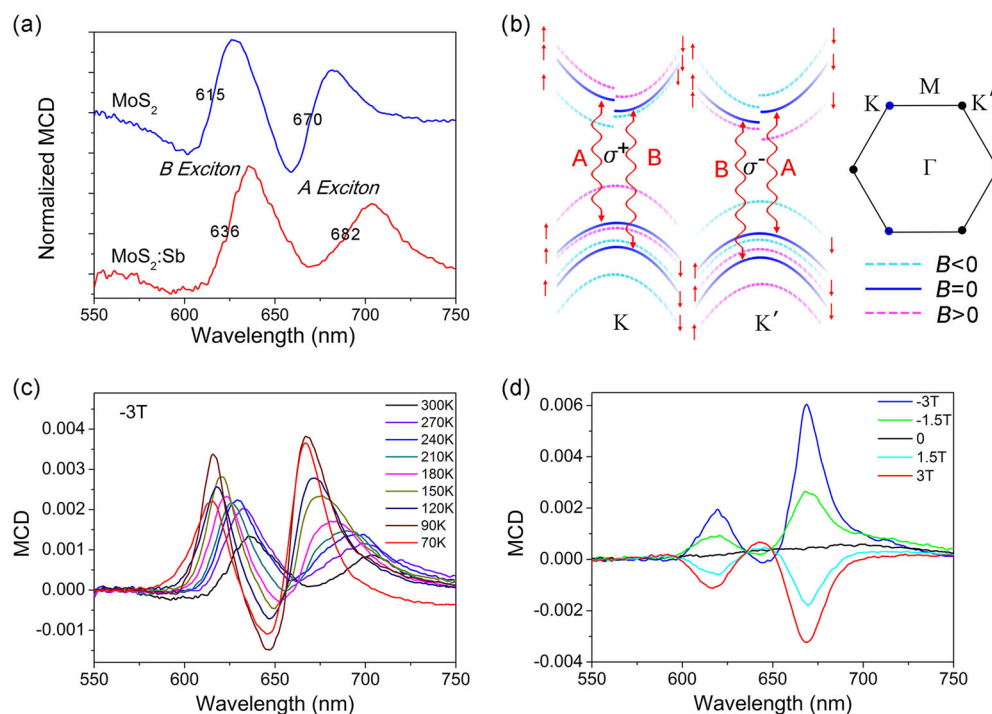


**Fig. 3** The characterization of A and B excitons. **a** Reflection magnetic circular dichroism (RMCD) spectra of monolayer Sb-doped MoS<sub>2</sub> and pristine MoS<sub>2</sub> crystals. The RMCD were performed at room temperature and the external field is  $-3\text{T}$ . **b** Schematic view of the splitting of electronic band structure at the K and K' points under the different applied magnetic fields ( $B \parallel \pm z$ ) due to the strong spin-orbit coupling. **c** Temperature-dependent RMCD spectra under  $-3\text{T}$  magnetic field, and **d** low-temperature (70 K) RMCD spectra under different magnetic fields of monolayer Sb-doped MoS<sub>2</sub>

The characterization of A and B excitons by reflection magnetic circular dichroism (RMCD) spectroscopy. Studies have shown that the RMCD spectroscopy is an effective tool to investigate the electronic band structure and magnetic properties of crystals.<sup>40–42</sup> More recently, the A and B excitons of

MoS<sub>2</sub> crystals are studied in detail by the RMCD.<sup>42</sup> The effect of Sb doping on MoS<sub>2</sub> were further confirmed by the RMCD results. The strong spin-orbit coupling in MoS<sub>2</sub> causes the spin degeneracy of electronic structures. The maximum splitting for the valence band appears at the K and K' points; while, at these points, the splitting

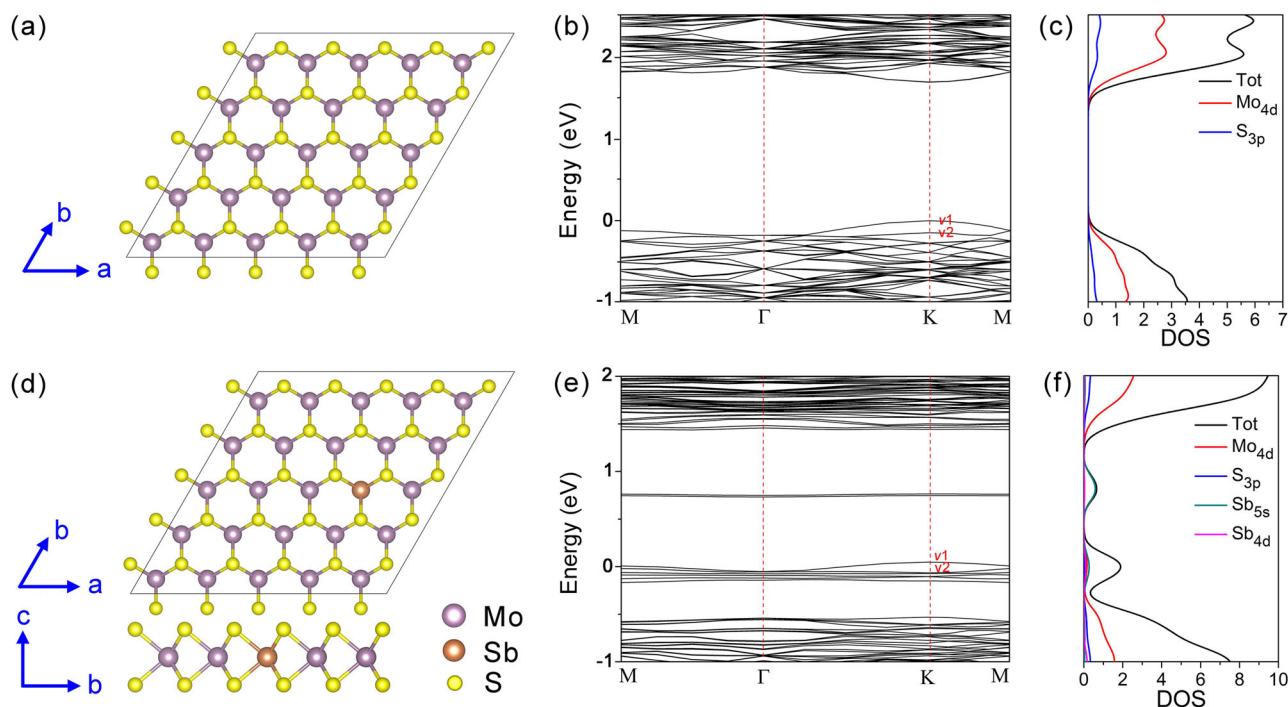


**Fig. 4** Electronic band structures calculated with PBE functional with spin-orbit coupling (SOC) effect. **a** The  $5 \times 5 \times 1$  supercell of  $\text{MoS}_2$ . **b** Electronic band structure of monolayer  $\text{MoS}_2$ . **c** Total density of states (TDOS) and orbital-projected density of states (PDOS) for Mo and S. **d** The  $5 \times 5 \times 1$  supercell of Sb-doped  $\text{MoS}_2$ . **e** Electronic band structure of monolayer Sb-doped  $\text{MoS}_2$ . **f** Total density of states (TDOS) and orbital-projected density of states (PDOS) for Mo, S, and Sb

of conduction band is very small (Fig. 3b). As a result, we will observe A and B excitons in PL, optical absorption spectrum, and optical reflection spectrum by some specific measurements.<sup>43</sup> As shown in Fig. 3a, the room-temperature RMCD spectrum from monolayer  $\text{MoS}_2$  and Sb-doped  $\text{MoS}_2$  single crystals display a similar shape, with A and B excitons observed in both crystals. For monolayer Sb-doped  $\text{MoS}_2$ , compared with  $\text{MoS}_2$ , the A exciton red shift about 21 nm and the B exciton red shift about 12 nm, respectively. The room-temperature RMCD results are very similar with the PL results.

Temperature-dependence of RMCD spectra for monolayer Sb-doped  $\text{MoS}_2$  are investigated in detail (Fig. 3c). With the decreasing temperature from 300 to 70 K, the peak positions of the A and B excitons undergo the significant blue-shifts. Meanwhile, the relative intensities of these two excitons have also changed clearly. For 300 K, the relative intensity of the B exciton is larger than the A exciton. As the temperature decreases, the intensity of the A and B excitons gradually increase. However, the intensity of A exciton increases faster than B exciton. When the temperature decreases to 70 K, the relative intensity of the A exciton becomes larger than the B exciton. Figure 3d shows the RMCD spectra of monolayer Sb-doped  $\text{MoS}_2$  under 70 K at different magnetic fields. The results show that two typical RMCD features (A and B excitons) are observed at non-zero field. But, the curves at different magnetic fields do not show the traditional symmetrical feature. This is mainly due to the limited quality of the tested crystal. The true reason may be more complicated, and more discussion is not given here.

## DISCUSSION

To understand the differences between monolayer  $\text{MoS}_2$  and Sb-doped  $\text{MoS}_2$  in PL and RMCD spectra, their electronic band structures are investigated by density functional theory (DFT) calculations. The  $5 \times 5 \times 1$  conventional unit cell is selected for the

studying of the pristine  $\text{MoS}_2$  (Fig. 4a) and Sb-doped  $\text{MoS}_2$  monolayer (Fig. 4d). The electronic band structure and density of states for pristine  $\text{MoS}_2$  monolayer from the PBE calculations including the spin-orbit coupling (SOC) effect are shown in Fig. 4b and c. The band gap of the pristine  $\text{MoS}_2$  monolayer is direct, with the conduction band minimum (CBM) and valence band maximum (VBM) located at the K point. We also can know that these states at the band edge mainly originate from the hybridization of S 3p and Mo 4d orbitals (Fig. 4c). Due to the SOC effect and the lack of inversion symmetry, the valence-band maximum has a large split (about 134 meV, they are  $K_{v1}$  and  $K_{v2}$ , respectively.), the CBM at K point also split but with a smaller splitting (3.7 meV, simply expressed as  $K_c$ ). The calculated band gaps from  $K_{v1}$  to  $K_c$  and  $K_{v2}$  to  $K_c$  are 1.71 and 1.85 eV, which are corresponding to the A and B excitons. The result is in well agreement with the previous studies and smaller than the value measured by RMCD (A exciton is 1.85 eV, B exciton is 2.01 eV) and PL (only A exciton is observed, the peak position at 1.86 eV).<sup>6</sup> Just like our case, the similar underestimation is also observed in the most TMDCs, which calculated by the conventional GGA-PBE method.

However, when the Mo atoms substituted by Sb atoms, the impurity energy levels appeared in band-gap. Here, the doping concentration is about 4% (one Mo atom is substituted by a Sb atom in a  $5 \times 5 \times 1$  supercell). We observed that the bands near the VBM originate from the hybridization between the Mo 4d, Sb 5s and 4d orbitals (Fig. 4f); among them, the Mo 4d orbital plays the main role. Meanwhile, two unoccupied impurity energy levels are formed at about 0.67 eV below the CBM, as illustrated in Fig. 4e. They mainly formed from the Sb 5s orbital (Fig. 4f). After doping, the band gap becomes smaller than the pristine one; the band gaps for Sb-doped  $\text{MoS}_2$  from  $K_{v1}$  to  $K_c$  and  $K_{v2}$  to  $K_c$  are 1.39 and 1.49 eV. So, it can illustrate the red-shifts of A and B excitons in the RMCD spectrum. In addition, due to the presence of these impurity energy levels, the transition process of non-equilibrium excess electrons is more complicated. Under the illumination of

light with wavelength smaller than the band gap, the electron in the valence band will be excited to the impurity energy level near the CBM and conduction band. After the light is turned off, the non-equilibrium excess electrons in the impurity energy level and conduction band will return to the valence band. Due to the band-impurity recombination, the probability of band-band recombination is reduced. So, the intensity of band-band radiation (PL) will be decreased. These calculation results qualitatively explain our experimental results of PL and RMCD.

In addition, the electronic transport properties of Sb-doped MoS<sub>2</sub> are also detailed investigated here. As shown in Supplementary Figure S9 and S10, the linear I-V curves indicate the formation of good ohmic contacts between Au electrodes and the prepared crystals. The typical field effect transistor based on the monolayer Sb-doped MoS<sub>2</sub> nanosheet exhibit a room-temperature electronic mobility of about 1.06 cm<sup>2</sup>/V·s (see Supplementary Figure S10a), which is larger than monolayer MoS<sub>2</sub> (0.56 cm<sup>2</sup>/V·s, see Supplementary Figure S9a) prepared using the same conditions as Sb-doped MoS<sub>2</sub>. Meanwhile, for monolayer Sb-doped MoS<sub>2</sub> FET, the carrier mobility has a peak value of about 1.8 cm<sup>2</sup> V<sup>-1</sup> s<sup>-1</sup> at about 100 K (see Supplementary Figure S11a and b). At low-temperature region, the carrier mobility is mainly limited by the impurity scattering. Above 100 K, the carrier mobility decreases rapidly with the increase of temperature in the form of  $\mu \sim T^{-\alpha}$ , where  $\alpha \approx 0.38$  (see Supplementary Figure S11b). This is due to lattice scattering dominates at this temperature region. But, the transition temperature of our prepared monolayer MoS<sub>2</sub> FET is about 260 K, and  $\alpha \approx 0.63$ , respectively (see Supplementary Figure S11c and d). The calculated electronic mobility of Sb-doped MoS<sub>2</sub> crystal is slightly larger than the purity monolayer MoS<sub>2</sub>, which may be related to the difference of defects and impurity concentrations in these two crystals. In 2D semiconductors, the possible scattering mechanisms are mainly acoustic and optical phonon scattering, Coulomb scattering at charged impurities, surface interface phonon scattering, and roughness scattering. The interaction of these scattering limit the carrier mobility. To this case, the doping of Sb in the MoS<sub>2</sub> system may decrease the density of defects. Moreover, the Sb-doping of MoS<sub>2</sub> crystals may have potential applications in multifunctional electronic and optoelectronic devices. More details can be found in Supplementary Discussion.

In summary, monolayer Sb-doped MoS<sub>2</sub> crystals successfully synthesized using a controllable CVD method. Growth time and carrier gas flow rate play the important role in controlling the layer and size of the final crystals. AC-STEM, HRTEM, and Raman spectroscopy results indicate that the Sb atoms are doped into MoS<sub>2</sub> by substitutionally replacing the Mo atoms in host lattice to form stable doping. EDS spectrum confirmed the stoichiometric ratio of Mo, Sb, and S is about 0.91:0.09:2, suggesting our fabricated crystals are Mo<sub>0.91</sub>Sb<sub>0.09</sub>S<sub>2</sub>. EDS and Raman mapping reveal that the spatial distribution of Mo, Sb, and S is homogeneous. According to the RMCD results, two excitons (A exciton and B exciton) are observed in the monolayer Mo<sub>0.91</sub>Sb<sub>0.09</sub>S<sub>2</sub> nanosheet, which have obviously position shifts compared with the monolayer MoS<sub>2</sub>. DFT calculations show the Sb doping results in the formation of impurity energy level in electronic band-gap of the pristine MoS<sub>2</sub>. It further confirmed by the shift of PL emission peak, and A and B excitons of monolayer Mo<sub>0.91</sub>Sb<sub>0.09</sub>S<sub>2</sub> nanosheet. The Sb-doped MoS<sub>2</sub> crystals may have potential applications in multifunctional electronic/optoelectronic and excitonic devices.

## METHODS

### Synthesis of monolayer MoS<sub>2</sub> and Sb-doped MoS<sub>2</sub> crystals

The monolayer MoS<sub>2</sub> and Sb-doped MoS<sub>2</sub> were grown on SiO<sub>2</sub>/Si substrate by a CVD process in a horizontal tube furnace. In a typical synthesis, 0.1 g pure sulfur powder, 0.06 g antimony powder, and 0.2 g molybdenum

trioxide powder were added to the ceramic boats as the source materials and placed at three different points of the furnace. Argon (Ar) is selected as the carrier gas. The substrates were placed on top of the ceramic boat loaded with molybdenum trioxide powder (Supplementary Figure S1a). The detailed heating conditions have been illustrated in Supplementary Figure S1b. In order to study the growth process, four growth times with 30 s, 1 min, 2 min, and 5 min have been applied. Before heating, high-purity Ar carrier gas was first introduced into the tube flow at 150 sccm for 30 mins to eliminate air in growth system, then the flow of Ar gas decrease to 3, 5, and 40 sccm for three different growth conditions, respectively. Finally, the furnace was cooled down to room temperature naturally. Meanwhile, increasing the gas flow rate of Ar rapidly expel the vapour in a remarkably short period of time.

### Fabrication of devices

The monolayer MoS<sub>2</sub> and Sb-doped MoS<sub>2</sub> based FETs fabricated on the SiO<sub>2</sub>/Si substrate (Si substrate with 300 nm SiO<sub>2</sub> insulating top layer) by the conventional lithography and electron-beam deposition, and lift-off process. The Au source and drain electrodes were deposited by electron beam evaporation. After removing the photoresist by acetone, the FETs were annealed under Ar atmosphere at 150 °C for 30 min to remove resist residue and decrease contact resistance.

### Measurement and characterization

The phase compositions, crystallographic structures, morphologies of the as-prepared materials were examined by optical microscope, high-resolution transmission electron microscopy (HRTEM; JEM-2100F, JEOL), and selected-area electron diffraction (SAED; JEM-2100F, JEOL), and energy dispersive X-ray spectroscopy (EDS; JEM-2100F, JEOL). Raman mapping, and photoluminescence (PL) spectra were collected using Renishaw inVia Reflex Raman Microscope and Spectrometer at the excitation line of 532 nm. The thicknesses of the prepared crystals were identified by atomic force microscopy (AFM, Nanoscope IIIa). Current-voltage (I-V) and the electron transport characteristics of the FETs were measured with transistor test system (Agilent-B2902). The excitons of purity and Sb-doped MoS<sub>2</sub> are measured with a home-built microscopic RMCD system. The applied magnetic field can be varied from -3 T to 3 T.

### Density functional theory calculations

First-principles calculations were performed using the projector augmented wave method with the generalized gradient approximation of Perdew-Burke-Ernzerhof (GGA-PBE) exchange-correlation functional including van der Waals corrections, as implemented in the Vienna ab initio simulation package.<sup>44-47</sup> The spin-orbit coupling effect is also considered in the calculation. All calculations are carried for a 5 × 5 × 1 supercell with 25 Mo atoms and 50 S atoms. A 15 Å vacuum layer is used to eliminate the interaction between adjacent images. By replacing one Mo atom with a Sb atom, the impurity concentration is set to 4%. Energy cutoff for plane-wave expansion was set to 450 eV. All the structures were fully relaxed using the conjugated gradient method until the Hellmann-Feynman force on each atom was less than 0.01 eV/Å.

## DATA AVAILABILITY

The data that support the findings of this study are available from the corresponding author upon reasonable request.

## ACKNOWLEDGEMENTS

This work was financially supported by the National Natural Science Foundation of China (grant no. 61622406, 11674310, 61571415, 51502283), the National Key Research and Development Program of China (Grant No. 2017YFA0207500), the Strategic Priority Research Program of Chinese Academy of Sciences (Grant No. XDB30000000), and the "Hundred Talents Program" of Chinese Academy of Sciences.

## AUTHOR CONTRIBUTIONS

Z.W. and J.L. designed the research. M.Z. and C.S. performed the experiments. L.H. performed the theory calculations. M.Z. wrote the paper. All authors had given approval to the final version of the manuscript. M.Z. and C.S. contributed equally to this work.

## ADDITIONAL INFORMATION

**Supplementary information** accompanies the paper on the *npj 2D Materials and Applications* website (<https://doi.org/10.1038/s41699-018-0083-1>).

**Competing interests:** The authors declare no competing interests.

**Publisher's note:** Springer Nature remains neutral with regard to jurisdictional claims in published maps and institutional affiliations.

## REFERENCES

- Ugeda, M. M. et al. Giant bandgap renormalization and excitonic effects in a monolayer transition metal dichalcogenide semiconductor. *Nat. Mater.* **13**, 1091–1095 (2014).
- Unuchek, D. et al. Room-temperature electrical control of exciton flux in a van der Waals heterostructure. *Nature* **560**, 340–344 (2018).
- Wang, Q. H., Kalantar-Zadeh, K., Kis, A., Coleman, J. N. & Strano, M. S. Electronics and optoelectronics of two-dimensional transition metal dichalcogenides. *Nat. Nanotechnol.* **7**, 699–712 (2012).
- Drapcho, S. G. et al. Apparent breakdown of Raman selection rule at valley exciton resonances in monolayer MoS<sub>2</sub>. *Phys. Rev. B* **95**, 5417–5417 (2017).
- Li, X. et al. Enhanced Nonlinear Optical Response of Rectangular MoS<sub>2</sub> and MoS<sub>2</sub>/TiO<sub>2</sub> in Dispersion and Film. *J. Phys. Chem. C* **120**, 18243–18248 (2016).
- Mak, K. F., Lee, C., Hone, J., Shan, J. & Heinz, T. F. Atomically thin MoS<sub>2</sub>: a new direct-gap semiconductor. *Phys. Rev. Lett.* **105**, 136805 (2010).
- Mak, K. F., McGill, K. L., Park, J. & McEuen, P. L. The valley Hall effect in MoS<sub>2</sub> transistors. *Science* **344**, 1489–1492 (2014).
- Splendiani, A. et al. Emerging photoluminescence in monolayer MoS<sub>2</sub>. *Nano. Lett.* **10**, 1271–1275 (2010).
- Yu, T. & Wu, M. W. Valley depolarization dynamics and valley Hall effect of excitons in monolayer and bilayer MoS<sub>2</sub>. *Phys. Rev. B* **93**, 045414 (2016).
- Zeng, H. L., Dai, J. F., Yao, W., Xiao, D. & Cui, X. D. Valley polarization in MoS<sub>2</sub> monolayers by optical pumping. *Nat. Nanotechnol.* **7**, 490–493 (2012).
- Xiao, D., Liu, G. B., Feng, W. X., Xu, X. D. & Yao, W. Coupled spin and valley physics in monolayers of MoS<sub>2</sub> and other group-VI dichalcogenides. *Phys. Rev. Lett.* **108**, 196802 (2012).
- Zhang, X., Lai, Z. C., Tan, C. L. & Zhang, H. Solution-processed two-dimensional MoS<sub>2</sub> nanosheets: preparation, hybridization, and applications. *Angew. Chem. Int. Ed.* **55**, 8816–8838 (2016).
- Radisavljevic, B., Radenovic, A., Brivio, J., Giacometti, V. & Kis, A. Single-layer MoS<sub>2</sub> transistors. *Nat. Nanotechnol.* **6**, 147–150 (2011).
- Lee, Y. H. et al. Synthesis of large-area MoS<sub>2</sub> atomic layers with chemical vapor deposition. *Adv. Mater.* **24**, 2320–2325 (2012).
- Lin, Y. C. et al. Wafer-scale MoS<sub>2</sub> thin layers prepared by MoO<sub>3</sub> sulfurization. *Nanoscale* **4**, 6637–6641 (2012).
- Schmidt, H. et al. Transport properties of monolayer MoS<sub>2</sub> grown by chemical vapor deposition. *Nano. Lett.* **14**, 1909–1913 (2014).
- Chen, W. et al. Oxygen-assisted chemical vapor deposition growth of large single-crystal and high-quality monolayer MoS<sub>2</sub>. *J. Am. Chem. Soc.* **137**, 15632–15635 (2015).
- Kang, K. et al. High-mobility three-atom-thick semiconducting films with wafer-scale homogeneity. *Nature* **520**, 656–660 (2015).
- Ataca, C. & Ciraci, S. Functionalization of single-layer MoS<sub>2</sub> honeycomb structures. *J. Phys. Chem. C* **115**, 13303–13311 (2011).
- Lin, X. Q. & Ni, J. Charge and magnetic states of Mn-, Fe-, and Co-doped monolayer MoS<sub>2</sub>. *J. Appl. Phys.* **116**, 044311 (2014).
- Dolui, K., Rungger, I., Das Pemmaraju, C. & Sanvito, S. Possible doping strategies for MoS<sub>2</sub> monolayers: an ab initio study. *Phys. Rev. B* **88**, 075420 (2013).
- Fuhr, J. D., Saul, A. & Sofo, J. O. Scanning tunneling microscopy chemical signature of point defects on the MoS<sub>2</sub>(0001) surface. *Phys. Rev. Lett.* **92**, 026802 (2004).
- Singh, N. & Schwingenschlogl, U. A route to permanent valley polarization in monolayer MoS<sub>2</sub>. *Adv. Mater.* **29**, 1600970 (2017).
- Cheng, Y. C., Zhu, Z. Y., Mi, W. B., Guo, Z. B. & Schwingenschlogl, U. Prediction of two-dimensional diluted magnetic semiconductors: doped monolayer MoS<sub>2</sub> systems. *Phys. Rev. B* **87**, 100401 (2013).
- Xu, E. Z. et al. p-Type transition-metal doping of large-area MoS<sub>2</sub> thin films grown by chemical vapor deposition. *Nanoscale* **9**, 3576–3584 (2017).
- Suh, J. et al. Doping against the native propensity of MoS<sub>2</sub>: degenerate hole doping by cation substitution. *Nano. Lett.* **14**, 6976–6982 (2014).
- Li, H. L. et al. Growth of alloy MoS<sub>2-x</sub>Se<sub>2(1-x)</sub> nanosheets with fully tunable chemical compositions and optical properties. *J. Am. Chem. Soc.* **136**, 3756–3759 (2014).
- Li, H. L. et al. Lateral growth of composition graded atomic layer MoS<sub>2(1-x)</sub>Se<sub>2x</sub> nanosheets. *J. Am. Chem. Soc.* **137**, 5284–5287 (2015).
- Dumcenco, D. O., Kobayashi, H., Liu, Z., Huang, Y. S. & Suenaga, K. Visualization and quantification of transition metal atomic mixing in Mo<sub>1-x</sub>W<sub>x</sub>S<sub>2</sub> single layers. *Nat. Commun.* **4**, 1351 (2013).
- Su, S. H. et al. Band gap-tunable molybdenum sulfide selenide monolayer alloy. *Small* **10**, 2589–2594 (2014).
- Bai, G. X. et al. 2D layered materials of rare-earth Er-doped MoS<sub>2</sub> with NIR-to-NIR down and up-conversion photoluminescence. *Adv. Mater.* **28**, 7472–7477 (2016).
- Li, B. et al. Synthesis and transport properties of large-scale alloy Co<sub>0.6</sub>Mo<sub>0.4</sub>S<sub>2</sub> bilayer nano sheets. *ACS Nano* **9**, 1257–1262 (2015).
- Gao, J. et al. Transition-metal substitution doping in synthetic atomically thin semiconductors. *Adv. Mater.* **28**, 9735–9743 (2016).
- Robertson, A. W. et al. Atomic structure and spectroscopy of single metal (Cr, V) substitutional dopants in monolayer MoS<sub>2</sub>. *ACS Nano* **10**, 10227–10236 (2016).
- Zhang, K. H. et al. Manganese doping of monolayer MoS<sub>2</sub>: the substrate is critical. *Nano. Lett.* **15**, 6586–6591 (2015).
- Del Alamo, J. A. Nanometre-scale electronics with III-V compound semiconductors. *Nature* **479**, 317–323 (2011).
- Pan, D. et al. Free-standing two-dimensional single-crystalline InSb nanosheets. *Nano. Lett.* **16**, 834–841 (2016).
- Zakaznova-Herzog, V. P. et al. High resolution XPS study of the large-band-gap semiconductor stibnite (Sb<sub>2</sub>S<sub>3</sub>): Structural contributions and surface reconstruction. *Surf. Sci.* **600**, 348–356 (2006).
- Zhong, M. et al. High-performance photodetectors based on Sb<sub>2</sub>S<sub>3</sub> nanowires: wavelength dependence and wide temperature range utilization. *Nanoscale* **9**, 12364–12371 (2017).
- Barrows, C. J., Vlaskin, V. A. & Gamelin, D. R. Absorption and magnetic circular dichroism analyses of giant Zeeman splittings in diffusion-doped colloidal Cd<sub>1-x</sub>Mn<sub>x</sub>Se quantum dots. *J. Phys. Chem. Lett.* **6**, 3076–3081 (2015).
- Muckel, F. et al. Digital doping in magic-sized CdSe clusters. *ACS Nano* **10**, 7135–7141 (2016).
- Wu, Y. et al. Valley Zeeman splitting of monolayer MoS<sub>2</sub> probed by low-field magnetic circular dichroism spectroscopy at room temperature. *Appl. Phys. Lett.* **112**, 153105 (2018).
- Mak, K. F., He, K., Shan, J. & Heinz, T. F. Control of valley polarization in monolayer MoS<sub>2</sub> by optical helicity. *Nat. Nanotechnol.* **7**, 494–498 (2012).
- Kresse, G. & Furthmüller, J. Efficient iterative schemes for ab initio total-energy calculations using a plane-wave basis set. *Phys. Rev. B* **54**, 11169 (1996).
- Kresse, G. & Furthmüller, J. Efficiency of ab-initio total energy calculations for metals and semiconductors using a plane-wave basis set. *Comput. Mater. Sci.* **6**, 15–50 (1996).
- Blöchl, P. E. Projector augmented-wave method. *Phys. Rev. B* **50**, 17953 (1994).
- Perdew, J. P., Burke, K. & Ernzerhof, M. Generalized gradient approximation made simple. *Phys. Rev. Lett.* **77**, 3865 (1996).



**Open Access** This article is licensed under a Creative Commons Attribution 4.0 International License, which permits use, sharing, adaptation, distribution and reproduction in any medium or format, as long as you give appropriate credit to the original author(s) and the source, provide a link to the Creative Commons license, and indicate if changes were made. The images or other third party material in this article are included in the article's Creative Commons license, unless indicated otherwise in a credit line to the material. If material is not included in the article's Creative Commons license and your intended use is not permitted by statutory regulation or exceeds the permitted use, you will need to obtain permission directly from the copyright holder. To view a copy of this license, visit <http://creativecommons.org/licenses/by/4.0/>.

© The Author(s) 2019